

# Technical note: Characterization, validation, and spectral optimization of a dedicated breast CT system for contrast-enhanced imaging

Juan J. Pautasso<sup>1</sup> | Koen Michielsen<sup>1</sup> | Ioannis Sechopoulos<sup>1,2,3</sup>

<sup>1</sup>Department of Medical Imaging, Radboud University Medical Center, Nijmegen, The Netherlands

<sup>2</sup>Dutch Expert Centre for Screening (LRCB), Nijmegen, The Netherlands

<sup>3</sup>Technical Medical Centre, University of Twente, Enschede, The Netherlands

## Correspondence

Ioannis Sechopoulos, Department of Medical Imaging, Radboud University Medical Center, Geert Grooteplein 10, 6525 GA, Post 766, Nijmegen, The Netherlands.  
Email: [ioannis.sechopoulos@radboudumc.nl](mailto:ioannis.sechopoulos@radboudumc.nl)

## Funding information

European Research Council (ERC) under the European Union's Horizon 2020 research and innovation programme, Grant/Award Number: 864929

## Abstract

**Background:** The development of a new imaging modality, such as 4D dynamic contrast-enhanced dedicated breast CT (4D DCE-bCT), requires optimization of the acquisition technique, particularly within the 2D contrast-enhanced imaging modality. Given the extensive parameter space, cascade-systems analysis is commonly used for such optimization.

**Purpose:** To implement and validate a parallel-cascaded model for bCT, focusing on optimizing and characterizing system performance in the projection domain to enhance the quality of input data for image reconstruction.

**Methods:** A parallel-cascaded system model of a state-of-the-art bCT system was developed and model predictions of the presampled modulation transfer function (MTF) and the normalized noise power spectrum (NNPS) were compared with empirical data collected in the projection domain. Validation was performed using the default settings of 49 kV with 1.5 mm aluminum filter and at 65 kV and 0.257 mm copper filter. A 10 mm aluminum plate was added to replicate the breast attenuation. Air kerma at the isocenter was measured at different tube current levels. Discrepancies between the measured projection domain metrics and model-predicted values were quantified using percentage error and coefficient of variation (CoV) for MTF and NNPS, respectively. The optimal filtration was for a 5 mm iodine disk detection task at 49, 55, 60, and 65 kV. The detectability index was calculated for the default aluminum filtration and for copper thicknesses ranging from 0.05 to 0.4 mm.

**Results:** At 49 kV, MTF errors were +5.1% and -5.1% at 1 and 2 cycles/mm, respectively; NNPS CoV was 5.3% (min = 3.7%; max = 8.5%). At 65 kV, MTF errors were -0.8% and -3.2%; NNPS CoV was 13.1% (min = 11.4%; max = 16.9%). Air kerma output was linear, with 11.67  $\mu\text{Gy}/\text{mA}$  ( $R^2 = 0.993$ ) and 19.14  $\mu\text{Gy}/\text{mA}$  ( $R^2 = 0.996$ ) at 49 and 65 kV, respectively. For iodine detection, a 0.25 mm-thick copper filter at 65 kV was found optimal, outperforming the default technique by 90%.

**Conclusion:** The model accurately predicts bCT system performance, specifically in the projection domain, under varied imaging conditions, potentially contributing to the enhancement of 2D contrast-enhanced imaging in 4D DCE-bCT.

This is an open access article under the terms of the [Creative Commons Attribution-NonCommercial](https://creativecommons.org/licenses/by-nc/4.0/) License, which permits use, distribution and reproduction in any medium, provided the original work is properly cited and is not used for commercial purposes.

© 2024 The Authors. *Medical Physics* published by Wiley Periodicals LLC on behalf of American Association of Physicists in Medicine.

**KEYWORDS**

cascaded system analysis, computed tomography, cone-beam breast CT, detectability index, flat panel detector

## 1 | INTRODUCTION

Since its inception in the 1970s, dedicated breast CT (bCT) technology has evolved significantly, particularly with the advent of flat-panel detectors (FPDs) and computational advances in the early 2000s.<sup>1</sup> This technology aims to overcome the limitations of 2D mammography by offering 3D imaging.<sup>2–7</sup> Recent studies even propose the feasibility of 4D dynamic contrast-enhanced bCT (4D DCE-bCT) for better lesion detectability and treatment personalization.<sup>8–12</sup> To optimize this advanced bCT modality, a comprehensive analysis of the parameter space is necessary. Cascaded-systems analysis, which breaks down the imaging process into discrete stages, offers an effective methodology for this optimization.<sup>13–26</sup>

Cascaded models have been utilized to guide the development of innovative imaging modalities, including full-field digital mammography,<sup>27–30</sup> tomosynthesis,<sup>31</sup> and dedicated cone-beam CT.<sup>32–35</sup> In this study, a parallel-cascaded model was implemented and validated to assess the performance of a dedicated bCT system compared to bCT measurements in the projection domain. Since the ultimate goal is to optimize bCT performance for 4D DCE-bCT, spectral optimization was performed within the projection domain. This entailed identifying optimal technique factors that enhance the iodine contrast signal. Specifically, we measured and modeled spatial resolution, noise, and detectability in the projection domain, employing the detectability index to navigate and optimize the relevant parameter space. This strategy ensures the provision of an optimized input for subsequent reconstruction processes, thereby potentially also enhancing the overall efficacy of 4D DCE-bCT imaging.<sup>36–40</sup>

## 2 | MATERIAL AND METHODS

### 2.1 | Dedicated breast CT system

A state-of-the-art dedicated bCT system (Koning Corp., Norcross, GA, USA) was used for this work (Figure 1). The system incorporates a pulsed x-ray tube and a FPD mounted on a rotating gantry. The x-ray tube (M-1581, Varian Medical Systems, Salt Lake City, UT) has a maximum anode heat capacity of 1.1 MJ and can operate at up to a maximum voltage of 70 kV with an inherent filtration of 1.4 mm Be. It uses a rotating anode with a 10° tilted tungsten coating insert and a nominal input power of 12 kW, with a nominal focal spot size of 0.3 mm. The

system allows for four voltage settings for the x-ray tube: 49 kV (default), 55, 60, and 65 kV. The tube current level is constrained by the system's maximum power capacity of 7 kW.

The mounted CMOS-based FPD is a Xineos 3030HS (Teledyne Dalsa, Waterloo, ON, CA) with 0.1518 mm pixel pitch and incorporates a CsI:TI columnar scintillator that is 0.700 mm thick. The active area spans 295 × 295 mm<sup>2</sup> involving 1952 × 1952 pixels. At full resolution, it is capable of a readout rate of 30 frames per second. Measured MTF nominal values have been reported to be 58% and 25% at 1 and 2 cycles/mm, respectively.<sup>35,41</sup> The source is located 950 mm from the detector (SDD) and 600 mm from the isocenter (SID). A standard bCT scan involves the acquisition of 225 projections over 360°, in 10 s.

### 2.2 | bCT measurements

The Modulation Transfer Function (MTF) and Noise Power Spectrum (NPS) of the aforementioned system were assessed in the projection domain. To accomplish this, the x-ray tube was configured to operate under standard bCT clinical settings: that is, voltage of 49 kV, pulse width of 5 ms, and a 1.5 mm additional aluminum filter of 99.999% purity. Additionally, a 10 mm thick aluminum plate, also with 99.999% purity, was placed at the x-ray tube's output to simulate the x-ray attenuation typically caused by a patient breast.



**FIGURE 1** Dedicated bCT system installed at Radboudumc and used for this work. The system has a length of 205 cm with a maximum width of 160 cm. The operating console, located to the right of this figure, comprises a standard computer and monitor with a user interface for image acquisition and reconstruction. bCT, breast CT.

### 2.2.1 | Presampled-MTF determination

To determine the presampled MTF of the bCT system, the edge method was utilized.<sup>42</sup> A tungsten edge test device (TX5, Ion Beam Applications SA, Louvain-La-Neuve, Belgium) was positioned at the entrance of the detector, angled slightly by approximately 3° and aligned with the x-ray beam's central ray.<sup>43</sup> The test edge was positioned to measure the vertical and horizontal MTFs, with a scout image acquired after each placement.

The acquired images were analyzed using the COQ plug-in, a specialized tool for ImageJ designed for the analysis of x-ray systems.<sup>44</sup> From 256 × 256 regions of interest (ROIs) encompassing a portion of the tungsten edge, both horizontal and vertical presampled MTFs were extracted. These MTFs were subsequently averaged to obtain the final bCT-measured MTF in the projection domain.

### 2.2.2 | Normalized NPS determination

Seven normalized Noise Power Spectra (NNPS) were measured in the projection domain using the bCT system, employing the same spectrum described above. These measurements were conducted at various tube current values: 20, 32, 40, 50, 64, 80, and 100 mA. Air kerma for each tube current was measured using an ion chamber connected to a dosimeter (10X6-6 chamber, 9660 ion chamber digitizer, and Accu-Pro 9660 control unit, Radcal Corp., Monrovia, CA, USA). The ion chamber was centered at the isocenter and aligned with the x-ray beam's central ray.

All acquired projection images were flat-field corrected through multiplication by the normalized reciprocal of the average intensity projection from the corresponding scan.

To calculate the NNPS, the COQ plug-in for ImageJ was again used. A 256 × 256 ROIs was used, aligned with the x-ray central beam axis, and included 14 lines (7 rows above and 7 below). This approach has shown good concordance with other methods described in existing literature.<sup>45</sup>

## 2.3 | Parallel-cascaded model

The developed model, shown in Figure 2, divides the bCT system's image formation process into eight stages, each characterized as linear, shift-invariant, and spatially stationary.<sup>13–26</sup> The two initial stages account for the interaction between x-rays and the scintillator, converting the x-rays into optical photons and incorporating K-fluorescent x-ray absorption through parallel

pathways. Subsequent stages focus on the processing of optical photons, from blurring effects to photodiode coupling and integration. The final stages cover the detector signal sampling and pixel readout. For any combination of input conditions, the output of the model consists of the estimates of the MTF and the NNPS.

### 2.3.1 | Stage 0: Incident x-rays

The polyenergetic x-ray spectrum was modeled using SpekPy software (v.2.0.8, October 2020) with the parameters described in Section 2.1.<sup>46</sup> Attenuation from 600 mm of air was accounted for to align the model with acquired data. An additional 350 mm of air attenuation and 2.5 mm of carbon fiber were added for the detector path. The scintillator's surface cover was modeled as 1 mm of silicon oxide. The stage's final output is the fluence in terms of energy and total fluence ( $q_0$ ) in photons/mm<sup>2</sup>.

### 2.3.2 | Stage 1: X-Rays interacting with the CsI:TI scintillator

The probability of an x-ray interacting with the scintillator follows a binomial process and is given by the average of the quantum efficiency  $\bar{g}_1$ .<sup>20</sup> The average quantum efficiency was computed as:

$$\bar{g}_1 = \int_0^{E_{\max}} g_1(E) q_{\text{rel}}(E) dE \quad (1)$$

The energy-dependent quantum efficiency ( $g_1(E)$ ) was weighted by the incident spectrum with  $q_{\text{rel}}(E)$  being the incident spectrum normalized by unit area.<sup>20</sup> The quantum efficiency  $g_1(E)$  is expressed as follows:

$$g_1(E) = 1 - \exp \left[ \left( \frac{\mu}{\rho}(E) \right)_{\text{CsI:TI}} \cdot t_{\text{CsI}} \cdot \rho_a \right] \quad (2)$$

The mass attenuation coefficient for CsI:TI was computed using the open source database XrayDB (v8.1 Python module 4.5.0, January 2023).<sup>47</sup> The thickness of the scintillator is denoted as  $t_{\text{CsI}}$ . The areal density ( $\rho_a$ ) is determined by multiplying the density of CsI ( $\rho_{\text{CsI}}$ ) with the packing factor ( $PF_{\text{CsI}}$ ). The density of CsI is 4.51 g/cm<sup>3</sup>, and the fractional weights for cesium ( $w_{\text{Cs}}$ ) and iodine ( $w_{\text{I}}$ ) in CsI are 0.51155 and 0.48845, respectively.<sup>48</sup> The packing factor,  $PF_{\text{CsI}}$ , was calculated based on the assumption of body-centered cubic unit cells for atoms of Cs and I.<sup>49</sup>

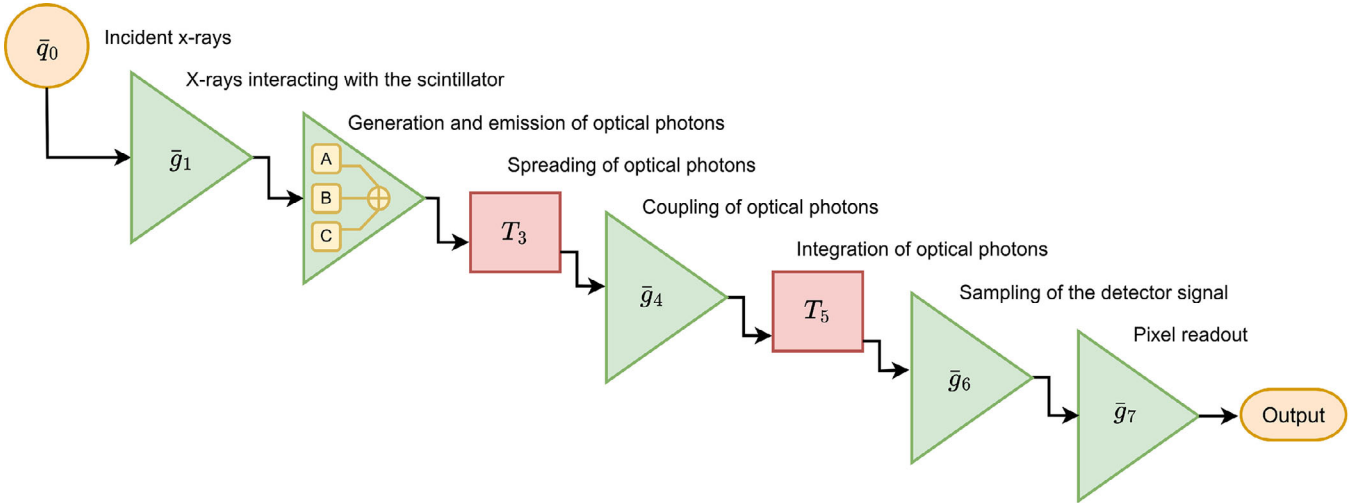


**FIGURE 2** Parallel-cascaded model representation as gain (triangles in green) and spreading (squares in red) stages.

### 2.3.3 | Stage 2: Generation and emission of optical photons

This stage involves three distinct light emission paths: A, B, and C, each with varying interactions with K-fluorescent x-rays. By following the works of Cunningham,<sup>18</sup> Yao<sup>19</sup> and Vedantham,<sup>20</sup> the average gain  $\bar{g}_2$  is expressed as:

$$\bar{g}_2 = (1 - \xi\omega) \bar{g}_{2A} + \xi\omega \bar{g}_{2B} + \xi\omega f_k \bar{g}_{2C} \quad (3)$$

The average gains along three light emission paths A, B, and C are calculated using the variables  $\xi$ ,  $\omega$ , and  $f_k$ , which represent K-shell photoelectric interaction probability, fluorescence yield, and fraction of K-fluorescent x-rays absorbed in the photodiode, respectively. Values for  $\xi$  and  $\omega$  are 0.83 and 0.87, obtained from Cao et al.<sup>34</sup> The K-fluorescent x-ray absorption factor,  $f_k$ , was calculated by applying the method developed by Chan and Doi.<sup>50</sup>

To compute the average gains for paths A, B, and C, the scintillator was partitioned into fractional layers each with a thickness of  $\Delta t$  as described by Vedantham et al.<sup>20</sup> Subsequent to this partitioning, the spreading of K-fluorescent photons, expressed as  $T_{ktotal}$ , was determined as:

$$T_{ktotal}(u, v) = \frac{(1 - \xi\omega) \bar{g}_{2A} + \xi\omega \bar{g}_{2B} + \xi\omega \bar{g}_{2C} f_k T_k(u, v)}{\bar{g}_2} \quad (4)$$

where  $T_k(u, v)$  is a transfer function describing K-edge x-ray reabsorption at varying distances. It was determined using Monte Carlo simulations considering the absorption and scattering coefficients for CsI:TI.<sup>20,51</sup> Attenuation coefficients corresponding to the average energy ( $E_K$ ) were obtained from the NIST database.<sup>52</sup>

During Monte Carlo simulations, the cylindrical response to an isotropic point source in a semi-infinite slab was calculated. Each photon undergoes hopping to a new position, weight dropping due to absorption, spinning into a new trajectory due to scattering, and a check to determine if the photon should terminate using the Roulette technique as detailed by Jacques.<sup>51,53</sup>

### 2.3.4 | Stage 3: Spreading of optical photons

The stochastic spread of optical quanta, denoted as  $T_3(u, v)$ , was fitted to the function:

$$T_3(u, v) = \frac{1}{1 + Hf^2 + H^2f^3} \quad (5)$$

In this equation,  $H$  serves as the fitting parameter and  $f$  represents the spatial frequency (cycles/mm).<sup>54</sup> This fitting parameter, also referred to as the blurring factor, was optimized using mean squared error, yielding an optimal value of 0.15. This optimization was carried out while considering all other components of the model as fixed.

### 2.3.5 | Stage 4: Coupling of optical photons to photodiode

This stage describes the stochastic gain that operates based on the binomial process. Within this process, the probability of an incident quantum being coupled to the photodiodes of the fiber optic plate is determined by the average coupling efficiency,  $\bar{g}_4$ . The specific value of  $\bar{g}_4$ , which is 0.48, was obtained from Cao et al.<sup>34</sup>



### 2.3.6 | Stage 5: Integration of optical photons by the photodiode

Stage 5 represents the deterministic spreading of optical quanta, characterize by the pixel presampling MTF<sup>20,24</sup>:

$$T_5(u, v) = \left| \text{sinc}(\pi a_x u) \text{sinc}(\pi a_y v) \right| \quad (6)$$

The light-sensitive pixel's active area is determined by  $a_x$  and  $a_y$ , derived from the pixel pitch ( $p_{pitch}$ ), and the fill factor ( $f_{pix}$ ).<sup>20,54</sup>

### 2.3.7 | Presampling MTF

At this instance of our model, the MTF at the detector can be formulated as proposed by Cao et al.<sup>34</sup>

$$\text{MTF}_{det}(u, v) = T_3(u, v) T_5(u, v) T_{k_{total}}(u, v) \quad (7)$$

### 2.3.8 | Stage 6: Sampling of the detector signal

Incorporating the work of Metz and Vyborny<sup>55</sup> and Vedantham,<sup>20,54</sup> the presampling NPS along the u-axis is defined by:

$$\begin{aligned} \text{NPS}_{pre}(u) &= \bar{q}_0 \bar{g}_1 \bar{g}_4 p_{pitch}^2 f_{pix} T_5^2(u) \\ &\left[ \bar{g}_4 T_3^2(u) \times (A(u) - \bar{g}_2) + \bar{g}_2 \right] \end{aligned} \quad (8)$$

Where:

$$\begin{aligned} A(u) &= (1 - \xi \omega) \bar{g}_{2A}^2 + \xi \omega \bar{g}_{2B}^2 + \xi \omega f_k \bar{g}_{2C}^2 \\ &+ 2\xi \omega f_k \bar{g}_{2B} \bar{g}_{2C} T_k(u). \end{aligned} \quad (9)$$

The pixel pitch and the fill factor are denoted as  $p_{pitch}$  and  $f_{pix}$ . The specific values for these parameters were set to 0.1518 and 0.85, respectively. Following this, Equation (10) introduces the comb function  $F_{III}$ , which characterizes the aliasing effect caused by the sampling of quantum noise.<sup>34</sup>

$$\text{NPS}_s = \text{NPS}_{pre} \otimes F_{III} \quad (10)$$

### 2.3.9 | Stage 7: Pixel readout

The last stage involves combining the aliased NPS with the power spectrum of the additive electronic noise, referred to as  $\text{NPS}_{add} = p_{pitch}^2 \sigma_{add}^2$ , to obtain the NPS

at the detector  $\text{NPS}_{det}$ :

$$\text{NPS}_{det} = \text{NPS}_s + \text{NPS}_{add} \quad (11)$$

### 2.3.10 | NNPS in projection images

As an extra step, the normalized NPS (NNPS) was expressed as follows:

$$\text{NNPS} = \frac{\text{NPS}_{det}}{L_{signal}^2} \quad (12)$$

Being  $L_{Signal}$  the large area signal defined as  $p_{pitch}^2 \bar{q}_0 \bar{g}_1 \bar{g}_2 \bar{g}_4$  as suggested by Cao et al.<sup>34</sup>

## 2.4 | Additional measurements for model validation

For a comprehensive validation of the developed parallel-cascaded model, the x-ray tube was also operated at a voltage of 65 kV with a pulse width of 5 ms. The standard 1.5 mm aluminum filter was replaced with a 0.257 mm copper filter, while retaining the same 10 mm aluminum plate to simulate a patient breast. The MTF and NNPS measurements in the projection domain were carried out as outlined in Sections 2.2.1 and 2.2.2, but the NNPS was measured at tube currents of 40, 50, 64, 80, and 100 mA. The choice of 65 kV and specified current levels is aimed at achieving high-quality pre-contrast images.

## 2.5 | Error calculation between bCT-measured and model-predicted MTFs

In order to calculate the discrepancy between the MTF values measured on the bCT system and those predicted by the model, the deviation at 1 and 2 cycles/mm, were examined. The error was calculated as follows:

$$\text{Error}(\%) = \frac{y_{predicted} - y_{measured}}{y_{measured}} \times 100 \quad (13)$$

where  $y_{predicted}$  and  $y_{measured}$  represents the model-predicted and the bCT-measured MTFs in the projection domain, respectively.

## 2.6 | Error calculation between bCT-measured and model-predicted NNPS

For the NNPS, the model's predictive performance was assessed by first calculating the residuals using the

root-mean-square error (RMSE):

$$RMSE = \sqrt{\frac{\sum_i^n (y_{predicted}^i - y_{measured}^i)^2}{n}} \quad (14)$$

where  $y_{predicted}$  and  $y_{measured}$  refer to the values predicted by the NNPS model and those measured by the bCT in the projection domain, respectively, while  $n$  stands for the total number of samples.

These values were then normalized by the average of the bCT-measured values for each case, resulting in the coefficient of variation (CoV), expressed as a percentage:

$$CoV(\%) = \frac{RMSE}{\bar{y}_{measured}} \times 100 \quad (15)$$

## 2.7 | Task-based spectral optimization

After characterizing the bCT system as described in Section 2.1 and validating the developed parallel-cascaded model, the model was used to determine the optimal spectral settings for imaging iodine with 4D DCE-bCT. For this, the parallel-cascaded model was first used with the x-ray tube voltage set to 49 kV, and the air kerma limited to 6 mGy. This limitation is imposed to ensure a fair comparison across thickness and tube-current settings. The breast was simulated with an average thickness of 80 mm, comprising 15% fibroglandular tissue and 85% adipose tissue, positioned at the isocenter.<sup>56,57</sup> These tissues were defined as having the chemical composition and density given by the NIST database.<sup>58</sup>

Iodine enhancement within breast lesions was modeled by integrating an iodine weight fraction ( $W_I$ ) based on a specified iodine concentration ( $C_I$ ) of 10 mg/mL, with consideration given to the distinct densities of breast tissue ( $\rho_{BN} = 1.02 \text{ g/cm}^3$ ) and iodine ( $\rho_I = 4.93 \text{ g/cm}^3$ ).<sup>58</sup> The weight fraction ( $W_I$ ) was calculated from the ratio of the mass of iodine ( $M_I$ ) in a given volume to the total mass of the breast tissue-iodine mixture ( $M_{Total}$ ), resulting in  $W_I = M_I/M_{Total}$ .

The adjusted density ( $\rho_{BI}$ ) was then estimated through a weighted average, reflecting the volume contributions of both iodine and the breast tissue. This was calculated as  $\rho_{BI} = (1 - V_I) \times \rho_{BN} + V_I \times \rho_I$  where  $V_I = \frac{C_I}{\rho_I}$  represented the proportion of iodine in the tissue.

For this analysis, initially a 1.5 mm aluminum filter was used, as per the default configuration. Subsequently, the performance with a copper filter was evaluated with it having thicknesses ranging from 0.05 to 0.4 mm with a 0.025 mm step.

The Modulation Transfer Function (MTF), large area signal ( $L_{signal}$ ), and Normalized Noise Power Spectrum (NNPS) were estimated for the breast without iodine, denoted as  $MTF_{BN}$ ,  $L_{signal_{BN}}$ , and  $NNPS_{BN}$  respectively, and for the breast with iodine, denoted as  $MTF_{BI}$ ,  $L_{signal_{BI}}$ , and  $NNPS_{BI}$ .

Given that the differences between the breast with and without iodine for MTF were minimal ( $MTF_{diff} < 0.1\%$ ), it was assumed that:

$$MTF = MTF_{BN} = MTF_{BI} \quad (16)$$

The NNPS was calculated as the sum of the NNPS values for the breast without and with iodine:

$$NNPS = NNPS_{BN} + NNPS_{BI} \quad (17)$$

The change in the signal ( $\Delta Signal$ ) due to iodine was calculated as:

$$\Delta Signal = L_{signal_{BI}} - L_{signal_{BN}} \quad (18)$$

A task was modeled to detect a disk with a 5 mm diameter. This is represented as:

$$W_{Task} = 2\pi \times r \times \text{sinc}(2\pi \times f \times r) \quad (19)$$

where the Fourier transform of a disk is approximated by a sinc function in 1D for simplicity, with being  $r$  the radius of the disk. Finally, the detectability index  $d'$  was calculated as the figure of merit along the spatial frequency axis ( $u$ ) up to the Nyquist frequency ( $u_{Nyq}$ ), as given by<sup>37</sup>:

$$d'^2 = \int_0^{u_{Nyq}} \frac{(MTF(u) \times \Delta Signal)^2}{NNPS(u)} W_{Task}^2(u) du \quad (20)$$

The analysis was subsequently performed with the tube voltage set to 55 kV, 60 kV, and 65 kV, the allowable tube voltage levels of the bCT system as described in Section 2.1. The detectability index obtained using the default aluminum filtration was then compared to the maximum  $d'$  achieved with the copper filter.

## 3 | RESULTS

### 3.1 | Model parameters

Table 1 lists the parameters used for the setup and tuning of the model. This table includes basic physical units, details on the geometry of the bCT system, and operating parameters for the detector.

**TABLE 1** Summary of terms and symbols and their corresponding values used in the parallel-cascaded model.

| Nomenclature                      | Notation       | Value                  | Ref. |
|-----------------------------------|----------------|------------------------|------|
| CsI:TI nominal thickness          | $t_{CsI}$      | 0.7 mm                 | —    |
| CsI density                       | $\rho_{CsI}$   | 4.91 g/cm <sup>3</sup> | 48   |
| Fractional weight of Cs in CsI    | $w_{Cs}$       | 0.51155                | 48   |
| Fractional weight of I in CsI     | $w_I$          | 0.48845                | 48   |
| Packing factor                    | $PF_{CsI}$     | 0.72                   | 49   |
| K-edge energy                     | $E_K$          | 35 keV                 | 34   |
| K-fluorescence probability        | $\xi$          | 0.83                   | 34   |
| K-fluorescent yield               | $\omega$       | 0.87                   | 34   |
| Work function                     | $m_0$          | 56 ph/keV              | 34   |
| Quantum detection efficiency      | $\tilde{g}_1$  | 0.9652                 | —    |
| K-fluorescence reabsorption       | $f_K$          | 0.75                   | —    |
| Coupling efficiency               | $\tilde{g}_4$  | 0.59                   | 34   |
| Blurring factor                   | H              | 0.15                   | —    |
| Fill factor                       | $f_{pix}$      | 0.85                   | —    |
| Pixel pitch                       | $p_{pitch}$    | 0.152 mm               | 41   |
| Electronic noise                  | $\sigma_{add}$ | 100 e <sup>-</sup> rms | —    |
| Fractional weight of I            | $W_I$          | 0.0097                 | —    |
| Breast tissue with iodine density | $\rho_{BI}$    | 1.03 g/cm <sup>3</sup> | —    |
| Source-detector distance          | SDD            | 950 mm                 | —    |
| Source-Isocenter distance         | SID            | 600 mm                 | —    |

### 3.2 | Air kerma and HVL measurements

The 1st HVL for the 49 kV spectrum with an added filtration of 1.5 mm Al was found to be 1.39 mm Al. After the introduction of the 10 mm Al aluminum plate, the HVL value increased to 3.55 mm Al.

When measurements were performed at 65 kV with additional filtration of 0.257 mm Cu, a 1st HVL of 4.47 mm Al was found. Then, upon introducing the 10 mm aluminum plate, the value rose to 5.87 mm Al. The air kerma values measured for 49 and 65 kV are presented in Figure 3.

### 3.3 | Validation at 49 kV

#### 3.3.1 | MTF at 49 kV

Figure 4 shows the presampled MTF measured at the detector at 49 kV, as outlined in Section 2.2.1, alongside the presampled MTF predicted by the implemented model. Analyzing the differences at two points, 1 and 2 cycles/mm, the calculated errors in percentage were +5.1% and −5.1%, respectively.

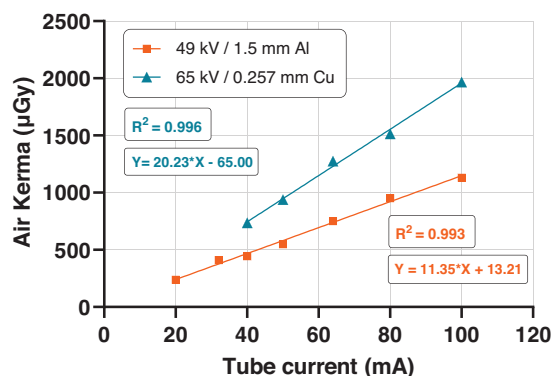


**FIGURE 3** Air kerma measurements for two distinct x-ray tube settings. For the first setting at 49 kV with a 1.5 mm Al filter measured air kerma values were 238, 410, 442, 548, 750, 952, and 1132 μGy, while the second setting at 65 kV with a 0.257 mm Cu filter yielded values of 736, 939, 1276, 1515, and 1967 μGy. Linear regression analysis shows  $R^2$  values at 0.993 and 0.996, respectively. The fitting parameters are  $Y = 11.35X + 13.21$  for 49 kV/1.5 mm Al, and  $Y = 20.23X - 65.00$  for 65 kV/0.257 mm Cu.

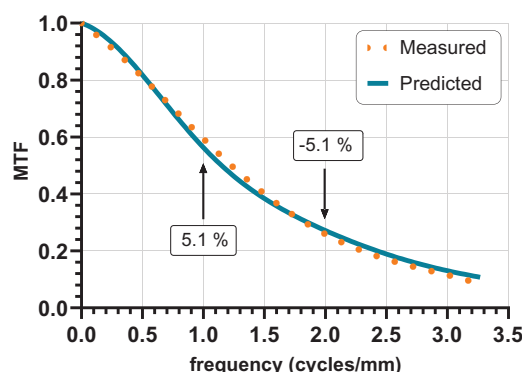


**FIGURE 4** bCT-measured at the detector (orange dots) and model-predicted (blue line) MTF plotted as a function of frequency. bCT, breast CT; MTF, modulation transfer function.

#### 3.3.2 | NNPS at 49 kV

In Figure 5, the NNPS measured at the detector and predicted by the model are shown. The mean CoV (min, max) was 5.3% (3.7%, 8.5%).

### 3.4 | Validation at 65 kV

#### 3.4.1 | MTF at 65 kV

Figure 6 shows the measured at the detector and modeled presampled MTF at 65 kV. The calculated errors at 1 and 2 cycles/mm were −0.8% and −3.2%.

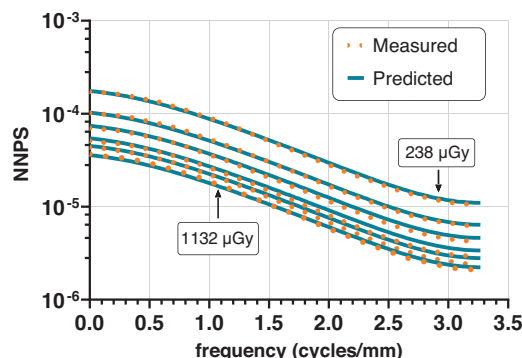


**FIGURE 5** bCT-measured at the detector (orange dots) and model-predicted (blue line) NNPS plotted as a function of frequency. From top to bottom the curves correspond to the air kerma measurements of 238, 410, 548, 750, 952, and 1132  $\mu\text{Gy}$ . bCT, breast CT; NNPS, normalized noise power spectrum.

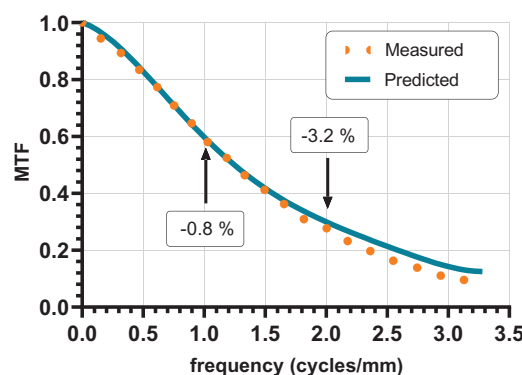


**FIGURE 6** MTF bCT-measured at the detector (orange dots) and model-predicted (blue line) plotted as a function of frequency. bCT, breast CT; MTF, modulation transfer function.

### 3.4.2 | NNPS at 65 kV

Figure 7 shows the bCT-measured at the detector and model-predicted NNPS. The computed mean value of the CoV was 13.1%, with a minimum and maximum of 11.4% and 16.9% respectively.

## 3.5 | Detectability index

The maximum iodine-detection  $d'$  was found to be when using an additional copper filtration 0.4 mm thick at 65 kV. However, the current required for the protocol of interest would exceed the system's power limitations (7 kW). Therefore, the optimum value was determined to be 0.25 mm of Cu. Figure 8 highlights the balance between  $d'$  and power consumption across varying copper thicknesses. For ease of comparison, the  $d'$  values are shown normalized to the maximum  $d'$ . The graph demonstrates a progressive improvement in  $d'$  with increasing copper filter thickness. This trend implies a

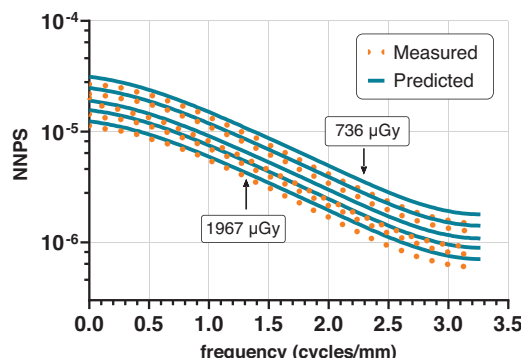


**FIGURE 7** bCT-measured at the detector (orange dots) and model-predicted (blue line) NNPS plotted as a function of frequency. From top to bottom the curves correspond to the air kerma measurements of 736, 939, 1276, 1515, and 1967  $\mu\text{Gy}$ . bCT, breast CT; NNPS, normalized noise power spectrum.

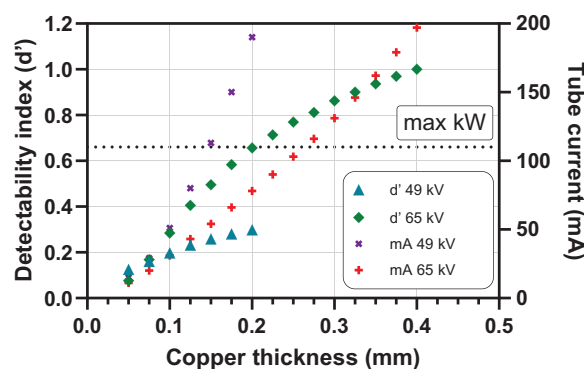


**FIGURE 8** Scatter plot illustrating the relationship between copper thickness and the detectability index ( $d'$ ) as well as the required tube current (mA) for the two voltage settings, 49 and 65 kV. Blue triangles and green diamonds represent the  $d'$  values at 49 and 65 kV, respectively. Purple and red crosses correspond to the tube current values at the respective voltage settings. The dotted line indicates the system's maximum power threshold ("max kW") at 65 kV.

sensitivity of  $d'$  to changes in filter thickness, where a greater thickness correlates with an enhanced  $d'$ .

At voltage settings of 49 and 55 kV, copper filtration outperformed 1.5 mm aluminum filtration. However, the system's power limitations restricted the maximum  $d'$ . At 60 kV, the highest  $d'$  was found at 0.225 mm Cu, but it was 19% lower than the observed at 65 kV/0.25 mm Cu.

When comparing the  $d'$  obtained for the default 1.5 mm aluminum filtration, the performance of the 65 kV/0.25 mm copper filter technique exceeds that obtained with 49 kV/1.5 mm Al and 65 kV/1.5 mm Al by 90% and 74%, respectively.

## 4 | DISCUSSION

In this work, a parallel-cascaded model to characterize a state-of-the-art dedicated bCT system was



implemented. The model allowed to derive the spatial frequency-dependent MTF and NNPS in the projection domain. The model predictions were validated with the aim of advancing 4D DCE-bCT and showed good agreement with measurements. Specifically, the discrepancies between the MTFs measured at the detector and those predicted by the model were approximately 5% at 49 kV and less than 5% at 65 kV. These results align with existing literature, as reported by Cao et al.<sup>34</sup> and Sheth et al.<sup>35</sup>

The model-predicted NNPS differed from the measured values by approximately 5% at 49 kV in terms of CoV. At 65 kV, however, the CoV rose to around 15%, likely due to the blurring factor being optimized for the default 49 kV tube voltage. This discrepancy is most evident at the tails of the NNPS curve, as seen in Figure 7. Future research could focus on optimizing a tube-voltage dependent blurring factor. The choice to utilize 49 kV with a 1.5 mm Al filter (default setting) and 65 kV with a 0.257 mm Cu filter was based on the evaluation of the x-ray tube's voltage range and the model's performance with different filtration.

The model is highly sensitive to even minor fluctuations in the output of number of photons, making it crucial to use measured input values rather than nominal values and a full stack of projections for NNPS measurements. This minimizes inconsistencies when comparing bCT-measured signals with model predictions given that the model assumes uniform behavior across projections. This premise could be undermined by variability in air kerma output between projections of the same scan.

Prior studies have made similar validation comparisons for cone-beam CT<sup>32–35</sup> and CMOS detectors,<sup>34,35</sup> with our results being consistent with those findings. Additionally, similar comparisons have been specifically performed for low-exposure values.<sup>20,28</sup> The results obtained are comparable to those published previously. Nevertheless, the distinct nature of the modeled systems, which are characterized by different components and input parameters, hinders direct comparisons between the curves representing spatial-frequency-dependent descriptors.

The calculation of the NNPS in our study, which entails summing the NNPS values for breast tissue both with and without iodine, draws on methodologies from Richard et al.'s work on dual-energy imaging systems. This approach, which adopts a subtraction factor ( $w_s$ ) of 1, is consistent with the optimization principles detailed in their analysis.<sup>59,60</sup> Additionally, it is important to clarify that our model does not incorporate anatomic noise. This means that our study employs a simplified approach in which a perfect alignment between the pre- and post-contrast images is achieved, resulting in complete removal of non-enhanced anatomic noise.

Furthermore, we recognize that the possible presence of background parenchymal enhancement (BPE)

would introduce an additional background iodine signal during contrast-enhanced breast imaging.<sup>61,62</sup> However, a spectral optimization as proposed in this study cannot distinguish the iodine signal uptake by a lesion from one in the parenchyma. Therefore, the findings here should be interpreted as an optimization, in the projection domain, of the detectability of iodine, not necessarily of an iodine-containing lesion. As evaluated by Day and Tanguay, BPE can significantly impact detectability, with reductions of up to 40% reported under certain conditions, depending on system and technique parameters.<sup>63,64</sup>

In this study,  $\Delta Signal$ , which measures the change in signal intensity due to iodine contrast, is adopted for a focused analysis of the contrast agent's effect. This approach enables the isolation of iodine's specific contribution to the overall signal, thereby offering a direct measure of contrast enhancement. The integration of  $\Delta Signal$  with the MTF and NNPS, both fundamental to the frequency domain, streamlined the analysis, eliminating the need to transform the large area signal ( $L_{Signal}$ ) from spatial to frequency domain.

The detectability index results facilitated the determination of the optimal tube voltage and filtering parameters for iodine detection with the bCT system evaluated.

These findings align with prior studies that optimized a bCT system with a different geometry and detector from those in the current investigation. Prionas et al. assessed six tube voltages (50, 60, 70, 80, 90, and 100 kV) and three different filters (0.2 mm Cu, 0.2 mm Sn, and 1.5 mm Al). They concluded that iodine contrast enhancement was optimized at 60 kV using a 0.2 mm Cu filter.<sup>36</sup> The differences between the values in this study and prior work are minimal; no detectability drop related to voltage was noted at 60 kV or 65 kV. Subsequently, Hernandez et al. found that a decrease in the signal-to-noise ratio with increasing tube voltage was significant only at 70 kV when using 0.2 mm Cu; 50 and 60 kV showed no notable difference.<sup>37</sup>

In separate studies, various materials were evaluated, and it was concluded that a 0.3 mm gadolinium filter would be a superior candidate to copper, surpassing its performance for iodine detection due to the K-edge at 50.2 keV. Despite gadolinium's advantages, copper's comparable performance, widespread availability, lower x-ray tube current requirements, and reduced manufacturing costs make it a good option for 4D DCE-bCT.<sup>37,38</sup>

Optimizing filter materials in the projection domain aims to enhance 3D reconstruction quality by providing high-quality inputs under the premise that any subsequent reconstruction method would be able to start from an optimized input.<sup>65</sup> However, this domain's insights might not capture all aspects of the 3D reconstruction process.<sup>66</sup> As a result, the benefits seen in 2D image quality from such optimizations do not guarantee similar

improvements in 3D reconstructions. This highlights the need for in-depth research into the effects of projection domain optimizations on 3D image quality in 4D DCE-bCT.

Moreover, the model was developed to work under default exposure time conditions, that is, a 5 ms pulse width with a 10-s scan time. The study did not investigate the effects of varying these parameters, leaving that for future research. An additional constraint within this study is that our findings are applicable to the specific system under evaluation. It is plausible that variations among seemingly identical systems, particularly in relation to input factors, may lead to disparities in subsequent outputs or results.

## 5 | CONCLUSION

A parallel-cascaded model was developed to characterize the response of a dedicated bCT system. The model demonstrated reasonable agreement with bCT measurements in predicting the system response, enabling efficient parameter optimization for 4D DCE-bCT development. The model highlights copper's practicality, though caution is warranted in extending 2D optimizations to more complex imaging.

## ACKNOWLEDGMENTS

This project has received funding from the European Research Council (ERC) under the European Union's Horizon 2020 research and innovation programme (grant agreement No 864929).

## CONFLICT OF INTEREST STATEMENT

Ioannis Sechopoulos is a Scientific Advisory Board member of Koning Corp.

## REFERENCES

- Gisvold JJ, Karsell PR, Reese EC. Clinical evaluation of computerized tomographic mammography. *Mayo Clin Proc.* 1977;52(3):181-185.
- Boone JM, Nelson TR, Lindfors KK, Seibert JA. Dedicated breast CT: radiation dose and image quality evaluation. *Radiology.* 2001;221(3):657-667. doi:[10.1148/radiol.2213010334](#)
- O'Connell A, Conover DL, Zhang Y, et al. Cone-beam CT for breast imaging: radiation dose, breast coverage, and image quality. *AJR Am J Roentgenol.* 2010;195(2):496-509. doi:[10.2214/AJR.08.1017](#)
- Sechopoulos I, Feng SS, D'Orsi CJ. Dosimetric characterization of a dedicated breast computed tomography clinical prototype [published correction appears in *Med Phys.* 2012;39(4):2314. *Med Phys.* 2010;37(8):4110-4120. doi:[10.1118/1.3457331](#)
- Sarno A, Mettivier G, Russo P. Dedicated breast computed tomography: basic aspects. *Med Phys.* 2015;42(6):2786-2804. doi:[10.1118/1.4919441](#)
- Zhu Y, O'Connell AM, Ma Y, et al. Dedicated breast CT: state of the art-Part I. Historical evolution and technical aspects. *Eur Radiol.* 2022;32(3):1579-1589. doi:[10.1007/s00330-021-08179-z](#)
- O'Connell AM, Marini TJ, Kawakyu-O'Connor DT. Cone-beam breast computed tomography: time for a new paradigm in breast imaging. *J Clin Med.* 2021;10(21):5135. doi:[10.3390/jcm10215135](#)
- Prionas ND, Lindfors KK, Ray S, et al. Contrast-enhanced dedicated breast CT: initial clinical experience. *Radiology.* 2010;256(3):714-723. doi:[10.1148/radiol.10092311](#)
- Prionas ND, Aminololama-Shakeri S, Yang K, Martinez SR, Lindfors KK, Boone JM. Contrast-enhanced dedicated breast CT detection of invasive breast cancer preceding mammographic diagnosis. *Radiol Case Rep.* 2015;10(2):936. doi:[10.2484/rcr.v10i2.936](#)
- Gazi PM, Aminololama-Shakeri S, Yang K, Boone JM. Temporal subtraction contrast-enhanced dedicated breast CT. *Phys Med Biol.* 2016;61(17):6322-6346. doi:[10.1088/0031-9155/61/17/6322](#)
- Caballo M, Mann R, Sechopoulos I. Patient-based 4D Digital Breast Phantom for perfusion contrast-enhanced breast CT imaging. *Med Phys.* 2018;45(10):4448-4460. doi:[10.1002/mp.13156](#)
- Caballo M, Michielsen K, Fedon C, Sechopoulos I. Towards 4D dedicated breast CT perfusion imaging of cancer: development and validation of computer simulated images. *Phys Med Biol.* 2019;64(24):245004. doi:[10.1088/1361-6560/ab55ac](#)
- Siewerdsen JH. Image quality models for 2D and 3D x-ray imaging systems: a perspective vignette. *Med Phys.* 2023;50(Suppl 1):109-116. doi:[10.1002/mp.16051](#)
- Antonuk LE, Jee KW, El-Mohri Y, et al. Strategies to improve the signal and noise performance of active matrix, flat-panel imagers for diagnostic x-ray applications. *Med Phys.* 2000;27(2):289-306. doi:[10.1118/1.598831](#)
- Cunningham IA, Moschandreou T, Subotic V. Detective quantum efficiency of fluoroscopic systems: The case for a spatial-temporal approach (or, does the ideal observer have infinite patience?). *Medical Imaging 2001: Physics of Medical Imaging, Proceedings of SPIE*; 2001. doi:[10.1117/12.430871](#)
- Cunningham IA, Yao J, Subotic V. Cascaded models and the DQE of flat-panel imagers: noise aliasing, secondary quantum noise, and reabsorption. *SPIE Proceedings.* 2002. doi:[10.1117/12.465610](#)
- Cunningham IA, Westmore MS, Fenster A. A spatial-frequency dependent quantum accounting diagram and detective quantum efficiency model of signal and noise propagation in cascaded imaging systems. *Med Phys.* 1994;21(3):417-427. doi:[10.1118/1.597401](#)
- Cunningham IA. Linear-systems modeling of parallel Cascaded Stochastic Processes: the NPS of radiographic screens with reabsorption of characteristic x-radiation. *SPIE Proceedings.* 1998. doi:[10.1117/12.317021](#)
- Yao J, Cunningham IA. Parallel cascades: new ways to describe noise transfer in medical imaging systems. *Med Phys.* 2001;28(10):2020-2038. doi:[10.1118/1.1405842](#)
- Vedantham S, Karellas A, Suryanarayanan S. Solid-state fluoroscopic imager for high-resolution angiography: parallel-cascaded linear systems analysis. *Med Phys.* 2004;31(5):1258-1268. doi:[10.1118/1.1689014](#)
- Rabbani M, Shaw R, van Metter R. Detective quantum efficiency of imaging systems with amplifying and scattering mechanisms. *J Opt Soc Am A.* 1987;4(5):895-901. doi:[10.1364/josaa.4.000895](#)
- Siewerdsen JH, Antonuk LE, el-Mohri Y, et al. Empirical and theoretical investigation of the noise performance of indirect detection, active matrix flat-panel imagers (AMFPIs) for diagnostic radiology. *Med Phys.* 1997;24(1):71-89. doi:[10.1118/1.597919](#)
- Siewerdsen JH, Antonuk LE, el-Mohri Y, Yorkston J, Huang W, Cunningham IA. Signal, noise power spectrum, and detective quantum efficiency of indirect-detection flat-panel imagers for diagnostic radiology. *Med Phys.* 1998;25(5):614-628. doi:[10.1118/1.598243](#)

24. Siewerdsen JH. *Signal, Noise, and Detective Quantum Efficiency of A-Si:H Flat-Panel Imagers*. The University of Michigan; 1998. [Doctoral dissertation].
25. Richard S, Siewerdsen JH. Cascaded systems analysis of noise reduction algorithms in dual-energy imaging. *Med Phys*. 2008;35(2):586-601. doi:10.1118/1.2826556
26. Zhao W, Ristic G, Rowlands JA. X-ray imaging performance of structured cesium iodide scintillators. *Med Phys*. 2004;31(9):2594-2605. doi:10.1118/1.1782676
27. Evans DS, Workman A, Payne M. A comparison of the imaging properties of CCD-based devices used for small field digital mammography. *Phys Med Biol*. 2002;47(1):117-135. doi:10.1088/0031-9155/47/1/309
28. Suryanarayanan S, Karellas A, Vedantham S, Sechopoulos I. Theoretical analysis of high-resolution digital mammography. *Phys Med Biol*. 2006;51(12):3041-3055. doi:10.1088/0031-9155/51/12/003
29. Williams MB, Simoni PU, Smilowitz L, Stanton M, Phillips W, Stewart A. Analysis of the detective quantum efficiency of a developmental detector for digital mammography. *Med Phys*. 1999;26(11):2273-2285. doi:10.1118/1.598741
30. Zhao W, Ji WG, Debie A, Rowlands JA. Imaging performance of amorphous selenium based flat-panel detectors for digital mammography: characterization of a small area prototype detector. *Med Phys*. 2003;30(2):254-263. doi:10.1118/1.1538233
31. Zhao B, Zhao W. Three-dimensional linear system analysis for breast tomosynthesis. *Med Phys*. 2008;35(12):5219-5232. doi:10.1118/1.2996014
32. Gang GJ, Lee J, Stayman JW, et al. Analysis of Fourier-domain task-based detectability index in tomosynthesis and cone-beam CT in relation to human observer performance. *Med Phys*. 2011;38:1754-1768.
33. Gang GJ, Zbijewski W, Webster Stayman J, Siewerdsen JH. Cascaded systems analysis of noise and detectability in dual-energy cone-beam CT. *Med Phys*. 2012;39(8):5145-5156. doi:10.1118/1.4736420
34. Cao Q, Sisniega A, Brehler M, et al. Modeling and evaluation of a high-resolution CMOS detector for cone-beam CT of the extremities. *Med Phys*. 2018;45(1):114-130. doi:10.1002/mp.12654
35. Sheth NM, Zbijewski W, Jacobson MW, et al. Mobile C-Arm with a CMOS detector: technical assessment of fluoroscopy and Cone-Beam CT imaging performance. *Med Phys*. 2018;45(12):5420-5436. doi:10.1002/mp.13244
36. Prionas ND, Huang SY, Boone JM. Experimentally determined spectral optimization for dedicated breast computed tomography. *Med Phys*. 2011;38(2):646-655. doi:10.1118/1.3537077
37. Hernandez AM, Abbey CK, Ghazi P, Burkett G, Boone JM. Effects of kV, filtration, dose, and object size on soft tissue and iodine contrast in dedicated breast CT. *Med Phys*. 2020;47(7):2869-2880. doi:10.1002/mp.14159
38. Glick SJ, Makeev A. Investigation of x-ray spectra for iodinated contrast-enhanced dedicated breast CT. *J Med Imaging*. 2017;4(1):013504. doi:10.1117/1.JMI.4.1.013504
39. Glick SJ, Thacker S, Gong X, Liu B. Evaluating the impact of X-ray spectral shape on image quality in flat-panel CT breast imaging. *Med Phys*. 2007;34(1):5-24. doi:10.1118/1.2388574
40. Weigel M, Vollmar SV, Kalender WA. Spectral optimization for dedicated breast CT. *Med Phys*. 2011;38(1):114-124. doi:10.1118/1.3523599
41. Teledyne Dalsa Xineos 3030HS. Xineos-3030HS. Teledyne DALSA. Accessed July 7, 2023. <https://www.teledynedalsa.com/en/products/imaging/medical-x-ray-detectors/xineos-large-area/xineos-3030hs/>
42. Samei E, Flynn MJ, Reimann DA. A method for measuring the presampled MTF of digital radiographic systems using an edge test device. *Med Phys*. 1998;25(1):102-113. doi:10.1118/1.598165
43. Samei E, Ranger NT, Dobbins JT 3rd, Chen Y. Intercomparison of methods for image quality characterization. I. Modulation transfer function. *Med Phys*. 2006;33(5):1454-1465. doi:10.1118/1.2188816
44. Donini B, Rivetti S, Lanconelli N, Bertolini M. Free software for performing physical analysis of systems for digital radiography and mammography. *Med Phys*. 2014;41(5):051903. doi:10.1118/1.4870955
45. Dobbins JT 3rd, Samei E, Ranger NT, Chen Y. Intercomparison of methods for image quality characterization. II. Noise power spectrum. *Med Phys*. 2006;33(5):1466-1475. doi:10.1118/1.2188819
46. Bujila R, Omar A, Poludniowski G. A validation of SpekPy: a software toolkit for modelling X-ray tube spectra. *Phys Med*. doi:10.1016/j.ejmp.2020.04.026. Published online June 5, 2020.
47. Xraydb. Accessed: July, 2023. <https://xraypy.github.io/XrayDB/python.html>
48. Hubbell J, Seltzer S. Tables of X-Ray Mass Attenuation Coefficients and Mass Energy-Absorption Coefficients 1 keV to 20 MeV for Elements Z = 1 to 92 and 48 Additional Substances of Dosimetric Interest. Radiation Physics Division, PML, NIST. 1995. Accessed July, 2023. <http://physics.nist.gov/PhysRefData/XrayMassCoef/cover.html>
49. Askeland DR, Wright WJ. *Essentials of Materials Science and Engineering*. 2nd ed. Cengage Learning; 2018:51-61.
50. Chan HP, Doi K. Energy and angular dependence of x-ray absorption and its effect on radiographic response in screen-film systems. *Phys Med Biol*. 1983;28(5):565-579. doi:10.1088/0031-9155/28/5/009
51. Jacques SL. Light distributions from point, line and plane sources for photochemical reactions and fluorescence in turbid biological tissues. *Photochem Photobiol*. 1998;67(1):23-32.
52. Chantler CT, Olsen KJ, Dragoset RA, Kishore AR, Kotochigova SA, Zucker DS. X-ray form factor, attenuation and scattering tables (version 2.0). 2003. Accessed July, 2023. <https://physics.nist.gov/PhysRefData/FFast/html/form.html>
53. Jacques SL, Prah SA. Steady-State Monte Carlo simulation. ECE532 Biomedical Optics. Oregon Graduate Institute; 1998. Accessed July 17, 2023. [omlc.org/classroom/ece532/class4/index.html](https://omlc.org/classroom/ece532/class4/index.html)
54. Vedantham S. *Design and Characterization of a High-Resolution Cardiovascular Imager*. Worcester Polytechnic Institute; 2002. [Doctoral dissertation]. MA.
55. Metz CE, Vyborny CJ. Wiener spectral effects of spatial correlation between the sites of characteristic x-ray emission and reabsorption in radiographic screen-film systems. *Phys Med Biol*. 1983;28(5):547-564. doi:10.1088/0031-9155/28/5/008
56. Pautasso JJ, Caballo M, Mikerov M, Boone JM, Michielsen K, Sechopoulos I. Deep learning for x-ray scatter correction in dedicated breast CT. *Med Phys*. 2023;50(4):2022-2036. doi:10.1002/mp.16185
57. Yaffe MJ, Boone JM, Packard N, et al. The myth of the 50-50 breast. *Med Phys*. 2009;36(12):5437-5443. doi:10.1118/1.3250863
58. ICRU. Tissue Substitutes in Radiation Dosimetry and Measurement. In: *Report 44 of the International Commission on Radiation Units and Measurements*. 1989.
59. Richard S, Siewerdsen JH. Optimization of dual-energy imaging systems using generalized NEQ and imaging task. *Med Phys*. 2007;34(1):127-139. doi:10.1118/1.2400620
60. Richard S, Siewerdsen JH, Jaffray DA, Moseley DJ, Bakhtiar B. Generalized DQE analysis of radiographic and dual-energy imaging using flat-panel detectors. *Med Phys*. 2005;32(5):1397-1413. doi:10.1118/1.1901203
61. Hill ML, Mainprize JG, Carton AK, et al. Anatomical noise in contrast-enhanced digital mammography. Part I. Single-energy imaging. *Med Phys*. 2013;40(5):051910. doi:10.1118/1.4801905

62. Hill ML, Mainprize JG, Carton AK, et al. Anatomical noise in contrast-enhanced digital mammography. Part II. Dual-energy imaging. *Med Phys*. 2013;40(8):081907. doi:[10.1118/1.4812681](https://doi.org/10.1118/1.4812681)
63. Hu YH, Scaduto DA, Zhao W. Optimization of contrast-enhanced breast imaging: analysis using a cascaded linear system model. *Med Phys*. 2017;44(1):43-56. doi:[10.1002/mp.12004](https://doi.org/10.1002/mp.12004)
64. Day JA, Tanguay J. Monte-Carlo study of contrast-enhanced spectral mammography with cadmium telluride photon-counting x-ray detectors. *Med Phys*. 2024;51:2479-2498. doi:[10.1002/mp.16837](https://doi.org/10.1002/mp.16837). Published online November 15, 2023.
65. Tward DJ, Siewerdsen JH. Noise aliasing and the 3D NEQ of flat-panel cone-beam CT: effect of 2D/3D apertures and sampling. *Med Phys*. 2009;36(8):3830-3843. doi:[10.1118/1.3166933](https://doi.org/10.1118/1.3166933)
66. Kijewski MF, Judy PF. The noise power spectrum of CT images. *Phys Med Biol*. 1987;32(5):565. doi:[10.1088/0031-9155/32/5/003](https://doi.org/10.1088/0031-9155/32/5/003)

**How to cite this article:** Pautasso JJ, Michielsen K, Sechopoulos I. Technical note: Characterization, validation, and spectral optimization of a dedicated breast CT system for contrast-enhanced imaging. *Med Phys*. 2024;1-12. <https://doi.org/10.1002/mp.17069>